Top Catal (2012) 55:955–968
DOI 10.1007/s11244-012-9881-4

ORIGINAL PAPER

Effect of Crystallographic Phase (β vs. γ) and Surface Area on Gas Phase Nitroarene Hydrogenation Over Mo_2N and Au/Mo_2N

Noémie Perret · Fernando Cárdenas-Lizana · Daniel Lamey · Vincent Laporte · Lioubov Kiwi-Minsker · Mark A. Keane

Published online: 21 August 2012

Abstract The catalytic action of Mo_2N and Au/Mo_2N has been assessed in the selective gas phase hydrogenation of *p*-chloronitrobenzene (*p*-CNB) to *p*-chloroaniline (*p*-CAN). The nitrides were synthesised via temperature programmed treatment of MoO_3 in $H_2 + N_2$ and Au introduced by deposition–precipitation with urea. We have examined the influence of nitride crystallographic phase (tetragonal β-Mo_2N vs. cubic γ-Mo_2N) and surface area (7–66 $m^2\ g^{-1}$) on the catalytic response. Catalyst activation by temperature programmed reduction has been monitored and the reduced catalysts characterised in terms of BET area/pore volume, H_2 chemisorption/temperature programmed desorption (TPD), powder X-ray diffraction (XRD), elemental analysis, scanning (SEM) and transmission (TEM) electron microscopy and X-ray photoelectron spectroscopy (XPS) measurements. The formation of β- and γ-Mo_2N was confirmed by XRD and TEM. γ-Mo_2N exhibits a platelet morphology whereas β-Mo_2N is characterised by an aggregation of small crystallites. Hydrogen chemisorption and TPD analysis have established a greater hydrogen uptake capacity (per unit area) for β-Mo_2N relative to γ-Mo_2N, which is associated with surface nitrogen deficiency, i.e. higher surface Mo/N for β-Mo_2N. Incorporation of Au on both nitrides resulted in an increase in surface hydrogen. The Au phase takes the form of *nano*-scale particles with a mean size of 7 and 4 nm on β-Mo_2N and γ-Mo_2N, respectively. Both β-Mo_2N and γ-Mo_2N promoted the exclusive hydrogenation of *p*-CNB to *p*-CAN where the β-form delivered a higher specific (per m^2) rate; the specific rate for γ-Mo_2N was independent of surface area. The inclusion of Au on both nitrides served to enhance *p*-CAN production.

Keywords Selective hydrogenation · *p*-Chloronitrobenzene · Surface area · Crystallographic phase · Molybdenum nitride · Au/Mo_2N

N. Perret · M. A. Keane (✉)
Chemical Engineering, School of Engineering and Physical Sciences, Heriot-Watt University, Edinburgh EH14 4AS, Scotland, UK
e-mail: M.A.Keane@hw.ac.uk

F. Cárdenas-Lizana (✉) · D. Lamey · L. Kiwi-Minsker
Group of Chemical Reaction Engineering, Ecole Polytechnique Fédérale de Lausanne, GGRC-ISIC-EPFL, Station 6, 1015 Lausanne, Switzerland
e-mail: fernando.cardenaslizana@epfl.ch

V. Laporte
Interdisciplinary Centre for Electron Microscopy, Ecole Polytechnique Fédérale de Lausanne, Station 12, 1015 Lausanne, Switzerland

1 Introduction

The application of transition metal nitrides as hydrotreating catalysts is now established [1–3]. The use of molybdenum nitride (Mo_2N) to promote hydrogen mediated reactions has been considered to a limited extent with evidence of significant hydrogenation activity [4–9]. This has been ascribed to a contraction of the *d*-band and modification of electron density due to the interstitial incorporation of N in the metal lattice, which facilitates hydrogen adsorption/activation [10]. A distinct selectivity response has been observed for Mo_2N when compared with conventional supported metal (e.g. Pd or Pt) catalysts [5, 6, 8]. Indeed, the preferential formation of crotyl alcohol (from crotonaldehyde) [6] and ethene (from ethyne) [5] has been reported for reaction over Mo_2N with enhanced selectivities relative to Pd/Al_2O_3. We have recently established the

synthesis of β-phase β-Mo_2N [8], with application in the selective hydrogenation of *p*-chloronitrobenzene (*p*-CNB) to *p*-chloroaniline (*p*-CAN) in both continuous gas [11] and batch liquid [11, 12] operation. *p*-CAN is a high value chemical extensively used in the manufacture of fine chemicals but existing production routes exhibit serious drawbacks in terms of low selectivity and the generation of toxic waste [13]. We have now extended the earlier work to consider the role of nitride crystallographic phase and surface area in gas phase hydrogenation.

In the synthesis of nitrides via temperature programmed reduction–nitridation, a number of factors have been proposed to influence the MoN_x phase, including the nature of the precursor [14] and preparation conditions [15–17], i.e. gas composition/space velocity, heating rate and final temperature. Cubic γ-Mo_2N has been the most common crystallographic form obtained via thermal treatment of MoO_3 in NH_3 [14, 15]. The use of $H_2 + N_2$ mixtures can generate either (tetragonal) β-Mo_2N [18–20] or γ-Mo_2N [16, 21, 22]. Moreover, the formation of (hexagonal) δ-MoN from $MoS_2 + NH_3$ has also been reported [23]. The synthesis of high surface area (up to 225 $m^2\ g^{-1}$) Mo_2N requires a low temperature ramp rate ($\leq$1 K min^{-1}) [16] and/or high gas space velocity (up to 150,000 h^{-1}) [24] to circumvent hydrothermal sintering resulting from water released [22]. β-Mo_2N typically exhibits low surface areas (2–17 $m^2\ g^{-1}$) [8, 19, 20] whereas higher values are characteristic of γ-Mo_2N (5–225 $m^2\ g^{-1}$) [25–27]. The effect of the nitride crystallographic phase in terms of hydrogenation applications has not been studied in a systematic manner. It is, however, worth noting that, in the case of ammonia synthesis [18] and carbazole hydrodenitrogenation [15], β-Mo_2N delivered a higher surface area normalised activity when compared with γ-Mo_2N and δ-MoN. A definitive correlation between catalytic activity and nitride area, irrespective of phase, has yet to be established. Hydrogen uptake, which is dependent on surface area and crystallographic phase [28–30], can play a critical role in determining hydrogenation rate. McKay and co-workers [18] have shown that specific activity (per m^2) for ammonia synthesis over β-Mo_2N was independent of surface area. In contrast, specific activities for thiophene desulfurisation [16] and pyridine hydrodenitrogenation [31] were found to decrease with increasing γ-Mo_2N area (from 4 to 193 $m^2\ g^{-1}$).

In this report, we consider for the first time the independent effect(s) of varying surface area (7–66 $m^2\ g^{-1}$) and Mo_2N crystallographic phase (β- and γ-) on *p*-CNB hydrogenation performance. Moreover, with a view to enhancing overall catalyst performance, we have assessed the role of Au as promoter. The use of promoters with Mo_2N catalysts has not been addressed to any significant extent. We should note that an increase in activity has been demonstrated for methanol steam reforming (with lower CO_2 production) over Mo_2N with the addition of Pd, Pt and Ni [32] and thiophene hydrodesulfurisation due to the inclusion of Co [33].

2 Experimental

2.1 Mo_2N Synthesis

The MoO_3 (99.9995 % w/w) precursor was obtained from Alfa Aesar. Mo_2N synthesis was conducted via temperature programmed treatment in H_2/N_2 or H_2/N_2/Ar continuous flow at atmospheric pressure. β-Mo_2N synthesis was carried out in a commercial CHEM-BET 3000 (Quantachrome) unit; γ-Mo_2N preparation employed a fixed bed reactor. As Mo_2N powders produced in reducing gases are subject to self-ignition on contact with air [34] resulting in a significant loss of surface area and modification to the crystal structure, the samples were passivated at 293 K in 1 % v/v O_2/He for *ex situ* analysis. There was no detectable temperature increase during passivation.

2.1.1 β-Mo_2N

The MoO_3 precursor was loaded in a quartz cell (3.76 mm i.d.) and contacted with 15 $cm^3\ min^{-1}$ (Brooks mass flow controlled; GHSV = 1,500 h^{-1}) H_2/N_2, kept at 293 K for 1 h and then heated at 5 K min^{-1} to 933 K, maintaining the final temperature for 18 h. The reaction was quenched by switching to an Ar flow (65 $cm^3\ min^{-1}$) and the sample was cooled to ambient temperature.

2.1.2 γ-Mo_2N

The MoO_3 precursor was placed in a horizontally mounted quartz reactor (i.d. = 10 mm), flushed with dry high purity Ar (99.9 % v/v) at 400 $cm^3\ min^{-1}$ (GHSV = 24,000 h^{-1}) for 4 h and heated to 623 K (at 5 K min^{-1}), which was maintained for 4 h. A 400 $cm^3\ min^{-1}$ flow of 8/42/50 % v/v N_2/H_2/Ar was then introduced and the temperature held constant for 2 h. Two γ-Mo_2N samples were prepared using different temperature ramping rates. The synthesis conditions were selected based on published literature [16] that has established a dependence of nitride surface area (34–101 $m^2\ g^{-1}$) on heating rate (0.2–20 K min^{-1}). The temperature was raised from 623 to 933 K at 0.3 K min^{-1} (sample denoted as γ-Mo_2N-a) or 0.1 K min^{-1} (γ-Mo_2N-b), maintaining the final isothermal hold for 2–13 h. The sample was quenched in Ar and rapidly (<30 min) cooled to ambient temperature; the latter step was facilitated by contacting the reactor with an external high velocity air flow.

2.2 Au/Mo_2N Preparation and Activation

Au/β-Mo_2N, Au/γ-Mo_2N-a and Au/γ-Mo_2N-b (with a nominal Au loading = 1 mol.%) were prepared by deposition–precipitation (D–P). A suspension of $HAuCl_4$ (300 cm^3, 3.32×10^{-4} M), aqueous urea (100 cm^3, 0.86 M) and the passivated nitride support (2 g), were stirred (300 rpm) and heated (1 K min^{-1}) to 353 K, maintaining the final temperature for 2.5 h. The D–P process was performed in the dark in order to avoid formation of metallic colloids in solution by photoreduction of Au(III) [35]. It has been reported that a high residual chloride content (>300 ppm) can induce the formation of large (>20 nm) Au particles [36] while the chloride can poison the catalytically active sites [37]. In order to circumvent these negative effects, the catalyst precursor was filtered, washed with distilled water until the wash water was Cl-free (based on the $AgNO_3$ test), dried in He (45 cm^3 min^{-1}) at 383 K for 3 h and sieved into a batch of 75 μm average particle diameter. The samples were kept at 277 K under He in the dark in order to prevent Au agglomeration, which has been reported for storage in air and in the light [38].

2.3 Characterisation

The pH values associated with the point of zero charge (pH_{PZC}) of the nitrides were determined using the potentiometric mass titration technique [39]. In each case, three different masses (0.025, 0.050 and 0.075 g) were immersed in 50 cm^3 0.1 M NaCl to which a known amount of NaOH (0.1 M) was added to adjust the pH to ca. 11. After stabilisation of the pH (ca. 1 h), titration of the samples was performed under continuous agitation in a He atmosphere with HCl (0.1 M). Temporal changes to pH were measured using a crystal-body electrode coupled to a data logging and collection system (Pico Technology Ltd.) where pH_{PZC} was obtained from the intersection of the temporal pH profiles. Calibration was performed with standard buffer solutions (pH 4 and 7). Temperature programmed reduction (TPR), BET surface area, total pore volume, H_2 chemisorption and temperature programmed desorption (TPD) were determined using the commercial CHEM-BET 3000 (Quantachrome) unit. The samples were loaded into a U-shaped Quartz cell (3.76 mm i.d.) and heated in 17 cm^3 min^{-1} (Brooks mass flow controlled) 5 % v/v H_2/N_2 at 2 K min^{-1} to 673 ± 1 K. The effluent gas passed through a liquid N_2 trap and changes in H_2 consumption were monitored by TCD with data acquisition using the TPR Win™ software. The activated samples were maintained at the final temperature in a constant flow of H_2/N_2 until return of the signal to baseline, swept with 65 cm^3 min^{-1} N_2 for 1.5 h and cooled to room temperature. The samples were then subjected to H_2 chemisorption using a pulse (10 μl) titration procedure, followed by H_2-TPD in N_2 (65 cm^3 min^{-1}) at 45 K min^{-1} to 933 K with an isothermal hold until the signal returned to the baseline. BET areas and pore volumes were determined, respectively, in 30 and 95 % v/v N_2/He using undiluted N_2 as internal standard. At least 3 cycles of N_2 adsorption–desorption in the flow mode were employed to determine total area and pore volume using the standard single point method. The measurements were reproducible to within ±8 % and the values quoted represent the mean.

Powder X-ray diffractograms were recorded on a Bruker/Siemens D500 incident X-ray diffractometer with Cu Kα radiation. The samples were scanned at a rate of 0.02° $step^{-1}$ over the range $20° \leq 2\theta \leq 90°$. Diffractograms were identified using the JCPDS-ICDD reference standards, i.e. MoO_3 (35-609), β-Mo_2N (25-1368), γ-Mo_2N (25-1366) and Au (04-0784). Lattice parameters and residual error associated with the main planes for β-Mo_2N and γ-Mo_2N were determined using the TOPAS (version 3) software. Analysis by scanning electron microscopy (SEM) was conducted on a Philips FEI XL30-FEG equipped with an Everhart–Thornley secondary-electron detector, operated at an accelerating voltage of 10–15 kV and using NORAN System SIX (version 1.6) for data acquisition. Before analysis, the samples underwent a hydrocarbon decontamination treatment using a plasma-cleaner (EVACTRON). Elemental (nitrogen) analyses were conducted using an Exeter CE-440 Elemental Analyser after sample combustion at ca. 1,873 K. The Au content was measured by atomic absorption spectroscopy (Shimadzu AA-6650 spectrometer with an air-acetylene flame) from the diluted extract in aqua regia (25 % v/v HNO_3/HCl). X-ray photoelectron spectroscopy (XPS) analyses were conducted on an Axis Ultra instrument (Kratos) using a monochromatic Al Kα X-ray source (1486.6 eV). Prior to analysis, the nitride sample was adhered to a conducting carbon tape, mounted in the sample holder and subjected to ultra-high vacuum conditions ($<10^{-8}$ Torr). The source power was maintained at 150 W and the emitted photoelectrons were sampled from a square area of 750 × 350 μm^2; the photoelectron take-off angle was 90°. The analyser pass energy was 80 eV for survey spectra (0–1,000 eV) and 40 eV for high resolution spectra (over the Mo $3d_{3/2}$ and Mo $3d_{5/2}$ binding energy (BE) range, 227–239 eV). Sputtering of the surface (for 1 min) with a 3 keV argon ion beam was employed to remove the passivating layer and reveal the sub-surface composition. The adventitious C 1 s peak was calibrated at 284.5 eV and used as internal standard to compensate for any charging effects. The instrument work function was calibrated to give a BE of 84.00 eV for the Au $4f_{7/2}$ line of metallic gold (Metalor) and the spectrometer dispersion was adjusted to give a BE of 932.70 eV for the Cu $2p_{3/2}$ line of metallic copper (Metalor). Quantification of the XPS signal employed the CasaXPS software, using relative sensitivity factors provided by

Kratos. High resolution transmission electron microscopy analyses were performed on a JEOL JEM 2011 unit with a UTW energy dispersive X-ray detector (Oxford Instruments) operated at an accelerating voltage of 200 kV; Gatan DigitalMicrograph 3.4 was employed for data acquisition. Samples for analysis were prepared by dispersion in acetone and deposited on a holey carbon/Cu grid (300 Mesh). Up to 320 individual Au particles were counted for each catalyst and the mean metal particle sizes are quoted as the number average (d_{TEM}).

2.4 Analytical Method and Catalytic System

2.4.1 Materials and Analytical method

All the gases (H_2 and N_2, Ar, O_2 and He) employed were of ultra high purity (>99.99, BOC). *p*-CNB (Sigma-Aldrich, ≥99 %) reactant and solvent (ethanol, Sigma Aldrich, ≥99.8 %) were used without further purification. The composition of the reactant/product mixtures was determined using a Perkin-Elmer Auto System XL chromatograph equipped with a programmed split/splitless injector and a flame ionisation detector, employing a DB-1 capillary column (i.d. = 0.33 mm, length = 30 m, film thickness = 0.20 μm). Data acquisition/manipulation was performed using the TotalChrom Workstation (Version 6.1.2 for Windows) chromatography data system. The overall reactant/product molar fractions were obtained using detailed calibrations (not shown).

2.4.2 Catalytic System

The hydrogenation of *p*-CNB was carried out under atmospheric pressure at 493 K, in situ immediately after activation, in a fixed bed vertical glass reactor (i.d. = 15 mm). The catalytic reactor was operated under conditions that ensured negligible heat/mass transport limitations. A layer of borosilicate glass beads served as preheating zone where the organic reactant was vaporised and reached reaction temperature before contacting the catalyst. Isothermal conditions (±1 K) were maintained by diluting the catalyst bed with ground glass (75 μm); the ground glass was mixed thoroughly with catalyst before insertion in the reactor. The reaction temperature was continuously monitored using a thermocouple inserted in a thermowell within the catalyst bed. The reactant (*p*-CNB as a solution in ethanol) was delivered at a fixed calibrated flow rate to the reactor via a glass/Teflon air-tight syringe and Teflon line using a microprocessor controlled infusion pump (Model 100 kd Scientific). A co-current flow of *p*-CNB and H_2 (<1 % v/v *p*-CNB in H_2) was delivered at a GHSV = 330 min^{-1} with an inlet reactant molar flow (F) in the range 0.7–3.2 μmol min^{-1}. The H_2 flow rate was monitored using a Humonics (Model 520) digital flowmeter, where the H_2 content was maintained well in excess of the stoichiometric requirement. The mass of catalyst to inlet *p*-CNB molar feed rate (m/F) spanned the range 2.6×10^{-3}–7.9×10^{-2} g min μmol^{-1}. As a blank test, passage of *p*-CNB in a stream of H_2 through the empty reactor did not result in any detectable conversion. The reactor effluent was frozen in a liquid nitrogen trap for subsequent analysis. Fractional hydrogenation ($X_{p\text{-CNB}}$) was obtained from

$$X_{p-\mathrm{CNB}} = \frac{[p-\mathrm{CNB}]_{\mathrm{in}} - [p-\mathrm{CNB}]_{\mathrm{out}}}{[p-\mathrm{CNB}]_{\mathrm{in}}} \quad (1)$$

and selectivity with respect to *p*-CAN, as the target product, is given by

$$S_{p-\mathrm{CAN}}\ (\%) = \frac{[p-\mathrm{CAN}]_{\mathrm{out}}}{[p-\mathrm{CNB}]_{\mathrm{in}} - [p-\mathrm{CNB}]_{\mathrm{out}}} \times 100 \quad (2)$$

Repeated reactions with different samples from the same batch of catalyst delivered conversion/selectivity values that were reproducible to within ±7 %.

3 Results and Discussion

3.1 Mo_2N

3.1.1 β-Mo_2N Characterisation

The XRD pattern of the MoO_3 precursor is shown Fig. 1a. The reflections over the range 2θ = 23–49° correspond to the (110), (040), (021), (130), (101), (111), (041), (060), (150), (061) and (002) planes that are characteristic of orthorhombic α-MoO_3 (JCPDS-ICDD 35-609, see Fig. 1e). The diffractogram for the passivated β-Mo_2N (Fig. 1b) shows peaks at 2θ = 37.7, 43.1, 45.3, 62.7, 64.3, 75.5, 78.6 and 80.5° that can be associated, respectively, with the (112), (200), (004), (220), (204), (312), (116) and (224) planes of β-Mo_2N (JCPDS-ICDD 25-1368, Fig. 1f). It should be noted that there were no detectable signals due to Mo or oxide species, a result that confirms the complete transformation of MoO_3 to β-Mo_2N, where the passivation step served solely to provide a superficial oxide film without bulk oxidation [19]. In order to check for a possible γ-phase content, the sample was subjected to a single crystal analysis using the TOPAS software for lattice parameter optimisation and the results are presented in Table 1. The residual error obtained from adjusting the *d*-spacing to tetragonal β-Mo_2N was significantly lower when compared with that obtained for cubic γ-Mo_2N. The lattice parameters from the adjustment to the β-form (a = 4.205; c = 8.045) are very close to those for the JCPDS-ICDD standard (25-1368). Moreover, the nitrogen

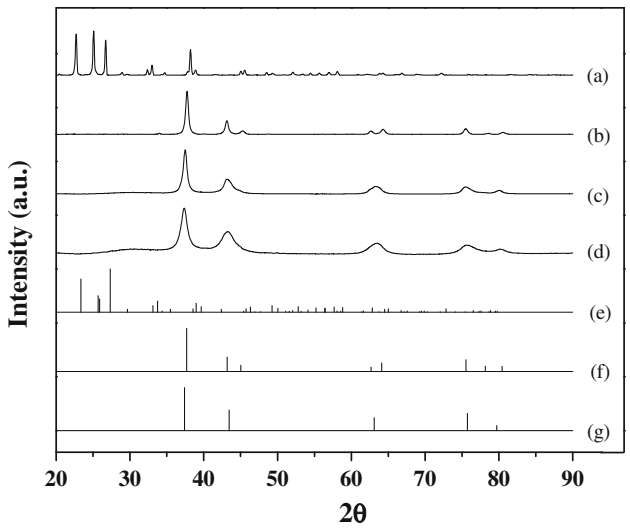

Fig. 1 XRD patterns associated with **a** MoO_3, **b** β-Mo_2N, **c** γ-Mo_2N-a and **d** γ-Mo_2N-b with JCPDS-ICDD reference diffractograms for **e** MoO_3 (35-609), **f** β-Mo_2N (25-1368) and **g** γ-Mo_2N (25-1366)

content (see Table 2: 5 % w/w, bulk Mo/N = 2.7) is in good agreement with reported values of 2.6–2.7 [18, 19, 40, 41] for β-Mo_2N.

The synthesised β-Mo_2N was examined by TEM and a representative image is shown in Fig. 21a where the intensity profile (see inset) yielded an average *d*-spacing of 0.24 nm, consistent with the (112) plane of β-Mo_2N. SEM analysis was also conducted to evaluate morphological features and the representative micrograph presented in Fig. 22a shows an aggregation of small crystallites (<5 μm). A β-Mo_2N crystal structure containing ensembles of varying sizes (<10 μm) has been reported elsewhere [14, 18, 20]. As the starting MoO_3 is characterised by a platelet morphology [42], the disruption of the orthorhombic precursor structure in the reduction/nitridation process ($MoO_3 \rightarrow MoO_2 \rightarrow Mo \rightarrow Mo_2N$) is the result of a non-topotactic transformation [8, 14, 19]. Cairns and co-workers [20] attributed the formation of small β-Mo_2N ensembles to water release/particle expansion during precursor reduction, following the model of Sloczynski and Bobinski [43]. It has been proposed [28] that passivation of Mo_2N results in the formation of one or two chemisorbed oxygen layers. Surface characterisation by XPS generated the spectra over the Mo 3*d* BE region for the MoO_3 precursor (a) and β-Mo_2N (b) presented in Fig. 3. The XPS profile for MoO_3 is characterised by a sole spin–orbit doublet with a Mo $3d_{3/2}$ BE = 236.6 eV that is characteristic of Mo^{6+} [44]. Removal of the passivating oxide layer from Mo_2N by Ar ion sputtering has been demonstrated elsewhere [44]. Sputtering was employed in this study to analyse the depth-profile composition of β-Mo_2N and mimic surface composition under reaction conditions. The XPS profile of the passivated sample (Fig. 3b1) shows a principal XPS peak at BE = 228.7 eV that is characteristic of $Mo^{\delta+}$ ($2 \leq \delta < 4$) in passivated β-Mo_2N [45–47]. The occurrence of a detectable signal at 236.4 eV is consistent with a partial oxidation to Mo^{6+} as a result of passivation [44]. While the hexavalent Mo signal in the precursor is strong and well defined, it is appreciably weaker for the Ar ion sputtered sample, demonstrating the near complete removal of the passivation layer (Fig. 3b2).

The temperature requirements for the removal of this oxide overlayer were analysed by TPR and the resultant profile, shown in Fig. 4a1, is characterised by a positive peak with a maximum intensity at 637 K. Hydrogen consumption

Table 1 Lattice parameters and residual error associated with the main planes for γ-Mo_2N and β-Mo_2N in the analysis of nitrides synthesised via temperature programmed treatment of MoO_3

Cubic γ-Mo_2N				Tetragonal β-Mo_2N			
h k l	Residual error (%)			h k l	Residual error (%)		
	β-Mo_2N	γ-Mo_2N-a	γ-Mo_2N-b		β-Mo_2N	γ-Mo_2N-a	γ-Mo_2N-b
1 1 1	0.532	0.257	0.315	1 1 2	0.079	0.196	0.163
2 0 0	1.018	0.326	0.129	2 0 0	0.099	0.783	1.235
2 2 0	1.134	0.101	0.285	0 0 4	0.005	–	–
3 1 1	0.693	0.079	0.047	2 2 0	0.013	–	–
2 2 2	0.492	0.280	0.332	2 0 4	0.082	1.334	0.942
				3 1 2	0.008	0.601	0.727
				1 1 6	0.016	–	–
				2 2 4	0.035	0.171	0.793
Lattice Parameters	a = 4.198	a = 4.163	a = 4.156	Lattice parameters	a = 4.205	a = 4.172	a = 4.162
					c = 8.045	c = 8.483	c = 8.201
	a* = 4.163				a** = 4.188 c** = 8.048		

* For JCPDS-ICDD γ-Mo_2N reference (25-1366); ** for JCPDS-ICDD β-Mo_2N reference (25-1368)

Table 2 Nitrogen content, Au loading, bulk and surface atomic Mo/N ratio, BET surface area, total pore volume, characteristic TPR T_{max} with associated H_2 consumption, H_2 chemisorbed/desorbed (TPD), pH of the point of zero charge (pH_{PZC}), Au particle size range and mean value (d_{TEM})

Catalyst	β-Mo_2N	Au/β-Mo_2N	γ-Mo_2N-a	Au/γ-Mo_2N-a	γ-Mo_2N-b	Au/γ-Mo_2N-b
Nitrogen content (% w/w)	5	–	6	–	6	–
Au loading (mol %)	–	0.26	–	0.54	–	0.59
Mo/N bulk ratio[a]; surface ratio after Ar ion sputtering[b]	2.7; 2.4	–	2.2; 1.4	–	2.2; 1.4	–
BET surface area ($m^2\ g^{-1}$)	7[c] (3)[d]	9[c] (5)[d]	36[c] (30)[d]	40[c] (33)[d]	66[c](60)[d]	82[c] (75)[d]
Pore volume ($cm^3\ g^{-1}$)	0.020	0.029	0.036	0.052	0.055	0.092
TPR T_{max} (K)	637	603	670	610	668	607
H_2 consumption during TPR ($\mu mol\ g^{-1}$)	303	373	732	777	1,292	1,454
H_2 chemisorption ($10^3\ \mu mol\ m^{-2}$)	42	45	16	20	16	18
TPD T_{max} (K)	806	746	827	795, 933	823	813, 933
H_2 desorbed ($\mu mol\ m^{-2}$)	0.4	1.4	0.2	0.7	0.2	0.5
pH_{PZC}	3.5	–	3.3	–	3.3	–
Au size range (nm)	–	2–13	–	1–8	–	1–8
d_{TEM} (nm)	–	7	–	4	–	4

[a] From elemental analysis

[b] From XPS measurements

[c] Activated sample

[d] Passivated sample

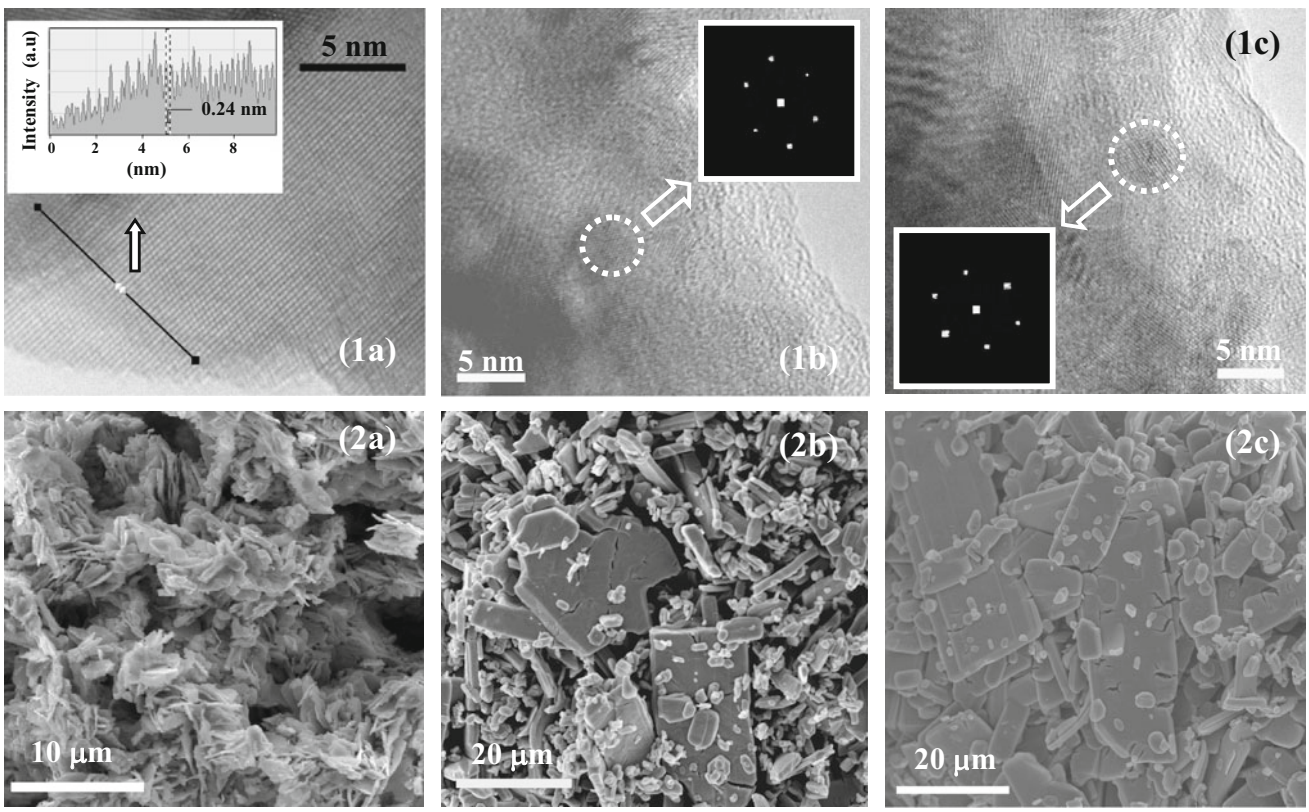

Fig. 2 Representative **1** TEM images and **2** SEM micrographs of *a* β-Mo_2N, *b* γ-Mo_2N-a and *c* γ-Mo_2N-b. *Inset* in *1a* shows the intensity profile, revealing the distance between the planes of the atomic lattice over the 10 nm segment that is marked on the TEM image; diffractogram patterns associated with the *circled areas* are included in (*1b*, *1c*)

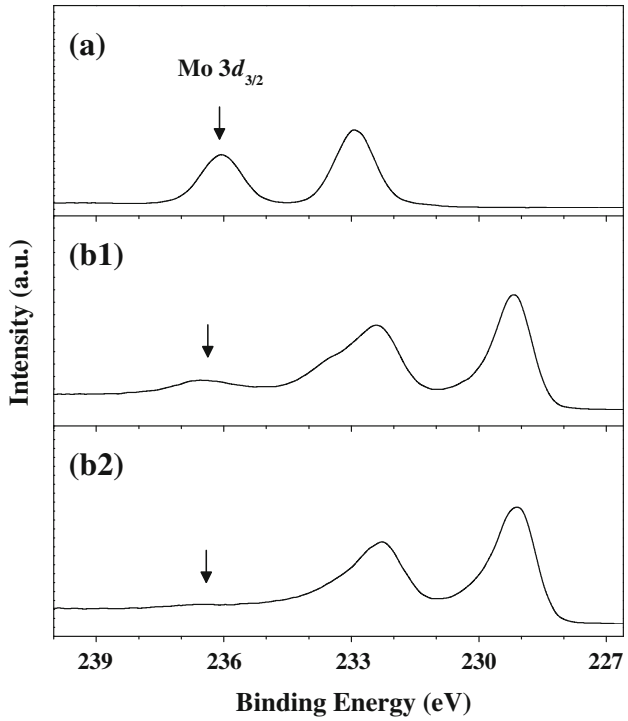

Fig. 3 XPS spectra in the Mo 3*d* region of **a** MoO_3 and **b** β-Mo_2N *1* passivated and *2* after Ar ion sputtering. *Arrows* illustrate the position of Mo $3d_{3/2}$ corresponding to Mo^{6+}

at temperatures over the range 637–740 K during TPR of passivated β-Mo_2N has been reported previously [11, 19, 28, 48]. The H_2 consumed (303 μmol g^{-1}) is recorded in Table 2 but we could not find any comparable measurement in the literature. The BET surface area falls within the range of values (2–17 m^2 g^{-1}) quoted previously for β-Mo_2N synthesised by temperature programmed reaction in N_2/H_2 [8, 18, 19]. The total area after passivation decreased (from 7 to 3 m^2 g^{-1}), as has been noted elsewhere [49]. A search through the literature has failed to unearth any study where quantitative measurements of H_2 chemisorption on β-Mo_2N are recorded. However, NMR [50] and IR [4] analyses suggest that H_2 can adsorb on Mo_2N at nitrogen deficient surface sites. Moreover, subsequent to adsorption, a heterolytic dissociation on Mo–N pairs (via the formation of Mo–H and N–H groups) has been proposed with migration to the sub-layers, which results in strong interactions [29, 30, 51]. A H_2 uptake of 42×10^{-3} μmol m^{-2} was recorded (Table 2) during pulse (ambient temperature) chemisorption analysis. Total surface hydrogen was evaluated by TPD and the resultant profile is presented in Fig. 5a1. The XRD pattern (not shown) of β-Mo_2N post-TPD was unchanged, demonstrating that the crystalline structure did not suffer any detectable alteration. Moreover, the nitrogen content (from elemental analysis) was also unchanged; it has been established that loss of nitrogen from β-Mo_2N requires temperatures in excess of 1,000 K [15]. The TPD profile is characterised by a broad peak (T_{max} = 806 K) where the H_2 released (0.4 μmol m^{-2}) is appreciably greater (by an order of magnitude) than that measured in the chemisorption step and must result from hydrogen uptake during TPR. Taking an overview of the limited available literature, the amount of H_2 desorbed (up to ca. 4 μmol m^{-2}) and associated T_{max} (370–800 K) appear to depend on nitride synthesis, pretreatment and surface area [28, 30]. High temperature (700–800 K) desorption has been associated with loss of H_2 from the bulk nitride as opposed to desorption from surface sites [30].

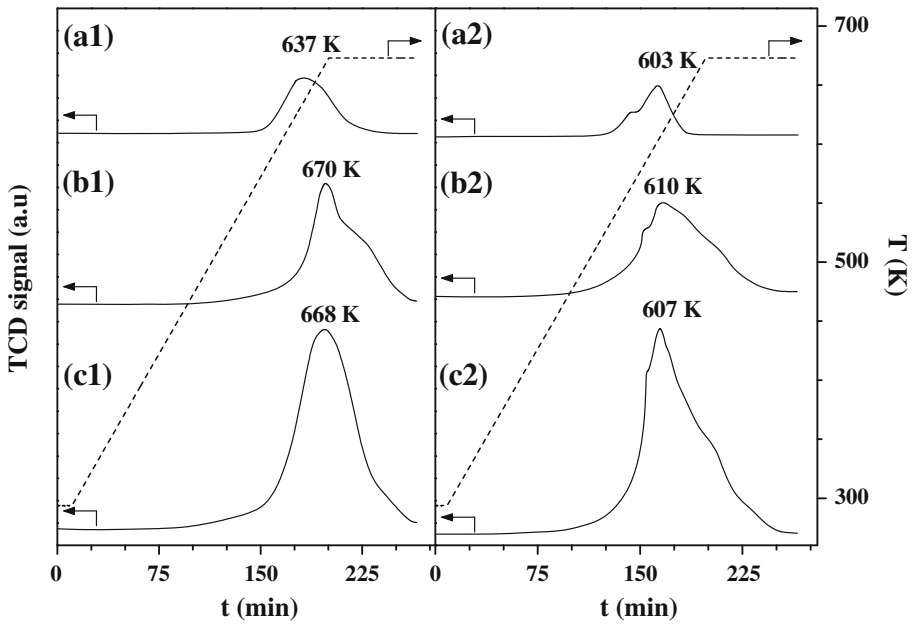

Fig. 4 TPR profiles (*solid line*) with temperature ramp (*dashed line*) generated for passivated **a** β-Mo_2N, **b** γ-Mo_2N-a and **c** γ-Mo_2N-b *1 pre-* and *2 post-*Au incorporation

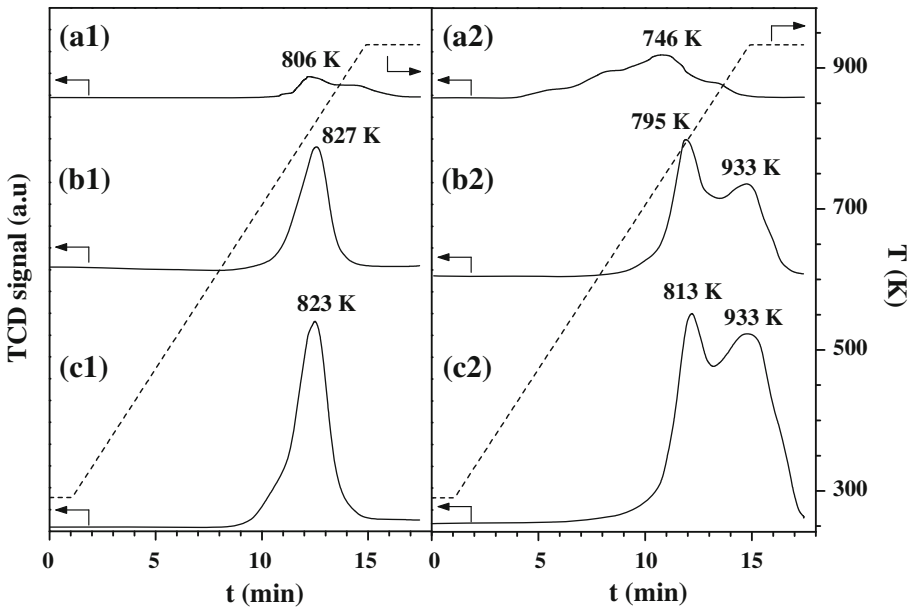

Fig. 5 Hydrogen TPD response (*solid line*) with temperature ramp (*dashed line*) for **a** β-Mo_2N, **b** γ-Mo_2N-a and **c** γ-Mo_2N-b *1* pre- and *2* post-Au incorporation

3.1.2 γ-Mo_2N Characterisation

Two γ-nitride (γ-Mo_2N-a and γ-Mo_2N-b) samples with different surface areas (Table 2) were synthesised by modifying the heating rate (see Sect. 2.1.2). The total pore volumes are comparable to those quoted by Zhang and co-workers [52], i.e. 0.012 $cm^3\ g^{-1}$ (surface area = 17 $m^2\ g^{-1}$) and 0.060 $cm^3\ g^{-1}$ (surface area = 110 $m^2\ g^{-1}$). A reduction in surface area was observed after passivation, as noted for β-Mo_2N. The nitrogen content of both γ-Mo_2N samples (Table 2) was equivalent (6 % w/w, bulk ratio Mo/N = 2.2) and agrees with values reported in the literature [46, 52]. The XRD patterns for γ-Mo_2N-a (c) and γ-Mo_2N-b (d) (see Fig. 1) coincide, presenting five main peaks at $2\theta = 37.5$, 43.6, 63.3, 76.0 and 80.0° that can be matched to the (111), (200), (220), (311) and (222) planes of cubic γ-Mo_2N [JCPDS-ICDD 25-1366, profile (g)]. Single crystal analysis generated lattice parameters consistent with the γ-Mo_2N JCPDS-ICDD standard; residual error < 0.4 % (Table 1). Representative TEM images of γ-Mo_2N-a and γ-Mo_2N-b are presented in Fig. 21b, 1c, respectively, where the *d*-spacings (0.20 and 0.24 nm) are in agreement with the (200) and (111) planes of γ-Mo_2N. SEM analysis (see Fig. 22b, 2c) has revealed the predominance of large (ca. 15 × 25 μm^2) platelet crystals with secondary, smaller (ca. 2 × 10 μm^2) rod-like formations. This suggests a retention of the platelet morphology characteristic of MoO_3 and a topotactic $MoO_3 \rightarrow Mo_xN_yO_{1-y} \rightarrow \gamma$-$Mo_2N$ transformation [25, 53]. The crystal size for both γ-Mo_2N samples is greater when compared with β-Mo_2N, as has been reported previously [18].

As in the case of β-Mo_2N, XPS analysis of γ-Mo_2N (not shown) confirmed a close to total removal of the passivation layer by Ar ion sputtering. A principal XPS signal at 228.3 eV was recorded that is within the range (228.2–230.0 eV) reported for passivated γ-Mo_2N [54–56] and attributed to $Mo^{\delta+}$ where $2 \leq \delta < 4$. In all three cases, bulk Mo/N exceeded the surface ratios (Table 2). Moreover, the surface Mo/N (1.4) for both sputtered γ-Mo_2N samples is significantly lower than that measured for β-Mo_2N (2.4). The TPR profiles recorded for passivated γ-Mo_2N-a (b1) and γ-Mo_2N-b (c1) shown in Fig. 4 are characterised by a peak at 669 ± 1 K that falls within the values (590–855 K) recorded elsewhere [28, 31, 57, 58]. A comparison of the TPR profiles for both γ-Mo_2N samples with that of β-Mo_2N reveals a shift in the reduction peak to a higher temperature (by ca. 30 K) for γ-Mo_2N, suggesting differences in oxygen-nitride interactions. The hydrogen consumed during TPR can be associated with (i) removal of the passivation layer and (ii) surface adsorption of H_2, which can migrate to sub-layers. Hydrogen consumption ($\mu mol\ g^{-1}$, see Table 2) increases in the order: β-Mo_2N < γ-Mo_2N-a < γ-Mo_2N-b. The hydrogen required for reduction of the passivation layer should be proportional to nitride surface area and an equivalent amount of H_2 (per surface area) was recorded for the two γ-Mo_2N (= 20 $\mu mol\ m^{-2}$) samples. This value is within the range (5–20 $\mu mol\ m^{-2}$) reported in the literature for γ-Mo_2N with BET areas of 24–193 $m^2\ g^{-1}$ [31]. The significantly higher specific H_2 consumption for β-Mo_2N (= 43 $\mu mol\ m^{-2}$) relative to (both) γ-Mo_2N can be related to the crystallographic structure (β- vs. γ-) where differences in the exposed planes and surface composition can affect oxygen interaction with the nitride surface. Moreover, there is some consensus [29, 50, 51, 59] that hydrogen uptake occurs at unsaturated surface Mo sites. Higher

H_2 consumption can then be related to the greater nitrogen deficient surface character (higher Mo/N) exhibited by β-nitride, as confirmed by XPS. Specific (per m^2) H_2 chemisorption (Table 2) was the same on both γ-Mo_2N samples but was significantly lower (by a factor of 3) than that recorded for β-Mo_2N. In contrast, Choi and co-workers [30] found that H_2 uptake capacity increased in the order, β-$Mo_{16}N_7$ < δ-MoN < γ-$Mo_{16}N_7$. They attributed this to a reduced number of Mo atoms on the surface of β-$Mo_{16}N_7$. We observe the opposite effect with a higher Mo/N surface ratio for β-Mo_2N relative to γ-Mo_2N. Hydrogen TPD from γ-Mo_2N-a (b1) and γ-Mo_2N-b (c1) generated the profiles presented in Fig. 5 with an equivalent H_2 release (0.2 μmol m^{-2}) at T_{max} = 825 ± 2 K, which is within the range (820–898 K) reported elsewhere [28, 60]. The shift in H_2 desorption to a higher temperature (by ca. 20 K) for γ-Mo_2N relative to β-Mo_2N suggests stronger interaction. Total H_2 desorbed from γ-Mo_2N was lower (by a factor of 2) than that recorded for β-Mo_2N, where the latter exhibited greater H_2 consumption (per surface area) in the TPR and chemisorption measurements. These results suggest a dependence of surface hydrogen content on crystallographic phase that can be linked to surface Mo/N.

3.1.3 Catalytic Results

Selectivity is the key challenge in the hydrogenation of *p*-CNB, i.e. exclusive –NO_2 group reduction without C–Cl bond scission. Dechlorination results in the formation of nitrobenzene (NB) with subsequent hydrogenation to aniline (AN) as shown in Fig. 6. Published articles [61–63] dealing with selective nitroarene hydrogenation have identified steps employed to improve selectivity, notably use of additives/promoters (e.g. NaHS and KOH) [64, 65], support modifications (in terms of Lewis acid–base properties and formation of oxygen vacancies) [66, 67] and metal dispersion [68]. Hydrogenation of *p*-CNB over β-Mo_2N, γ-Mo_2N-a and γ-Mo_2N-b generated *p*-CAN as the sole product, with no evidence of dechlorination. This finding in itself is significant as composite hydrodechlorination/hydrogenation (to form NB/AN) is a feature of reaction over conventional transition metal catalysts, i.e. Ni [69], Pt [70] and Ru [71]. Hydrogenation selectivity can be attributed to effective polarisation of the N=O group via surface interaction that renders the nitro function susceptible for hydrogen attack [72]. Indeed, –NO_2 adsorption-reduction on Mo has been demonstrated elsewhere [73, 74] and Chen and Chen [69] have shown that the addition of Mo to nickel borides promoted selective nitro-group reduction while suppressing the dehalogenation step.

A temporal decrease in fractional *p*-CNB conversion ($X_{p\text{-CNB}}$) with time on-stream was observed, which can be expressed in terms of the empirical relationship [75]

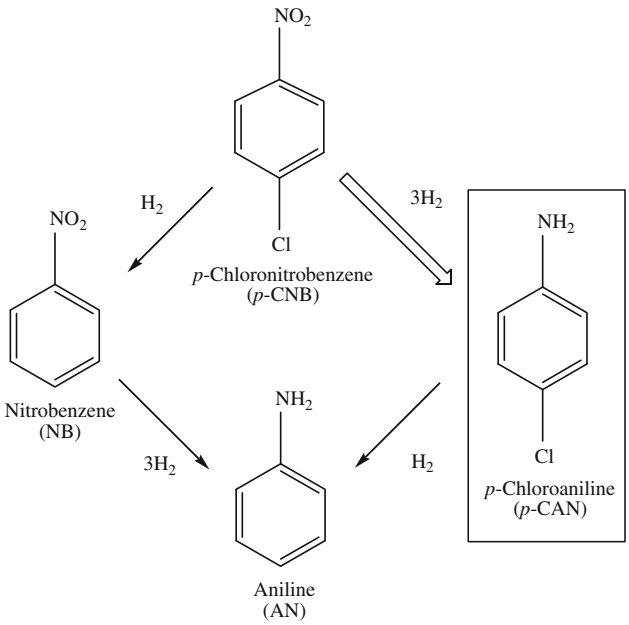

Fig. 6 Main reaction pathways associated with the hydrogenation of *p*-CNB to the target (⇨) product (*p*-CAN) with non-selective (*solid arrow*) products resulting from hydrodechlorination/hydrogenation

$$\frac{(X_{p-\text{CNB}} - X_0)}{(X_{30\text{h}} - X_0)} = \frac{t}{(\beta + t)} \tag{3}$$

from which a value for the initial conversion (X_0) can be obtained, where $X_{30\ \text{h}}$ represents fractional conversion after 30 h on-stream and β is a time scale fitting parameter. A representative (β-Mo_2N) time on-stream response is shown in Fig. 7a where it can be noted that a near steady state conversion was attained after ca. 15 h and maintained for 30 h of continuous operation. The applicability of a pseudo-first order kinetic treatment has been established for related catalyst systems [75].

$$\ln(1 - X_0)^{-1} = k\left(\frac{m}{F}\right) \tag{4}$$

where *m/F* corresponds to the mass of catalyst relative to inlet *p*-CNB molar feed rate. The pseudo-first order kinetic plots for β-Mo_2N, γ-Mo_2N-a and γ-Mo_2N-b are included in Fig. 7b–d. The linear fit (passing through the origin) confirms adherence to the kinetic model. The extracted raw rate constants (k, μmol g^{-1} min^{-1}, Table 3) follow the order, γ-Mo_2N-b > γ-Mo_2N-a > β-Mo_2N. In order to differentiate between the effect of surface area and crystal phase on the catalytic activity, the comparison must be based on specific rate (k', μmol m^{-2} min^{-1}, Table 3). Both γ-Mo_2N-a and γ-Mo_2N-b delivered an equivalent specific activity (35 ± 2 × 10^{-2} μmol m^{-2} min^{-1}) demonstrating that, for a given crystallographic phase, the intrinsic activity is independent of surface area. A significant finding is the appreciably higher specific rate recorded for

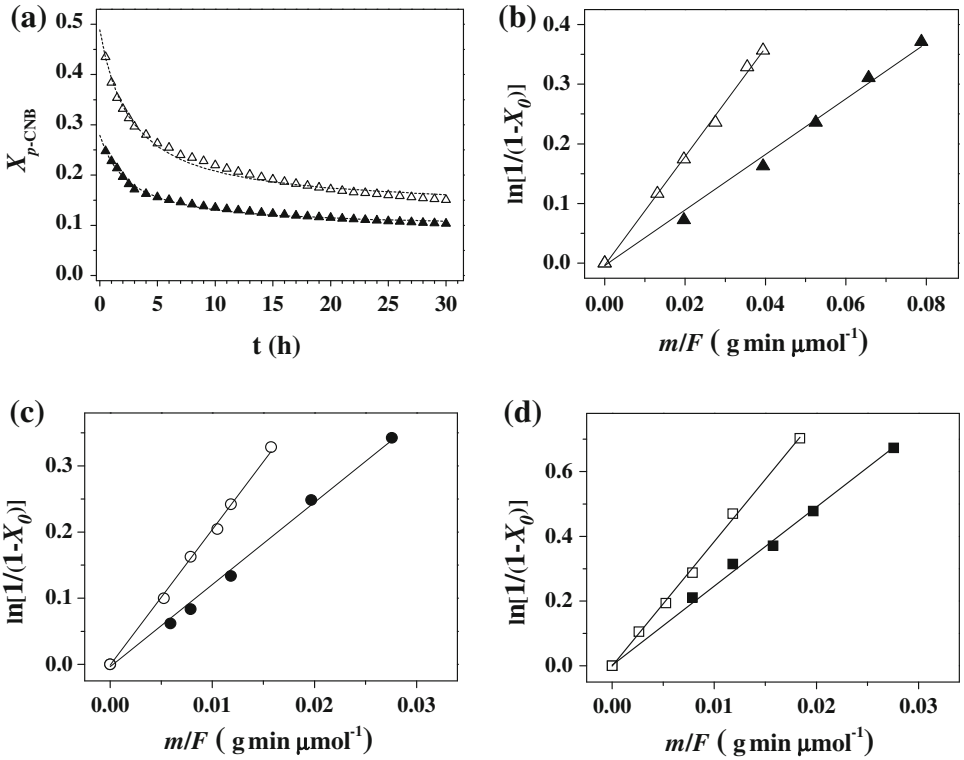

Fig. 7 **a** Variation of *p*-CNB fractional conversion ($X_{p\text{-CNB}}$) with time-on-stream ($m/F = 0.08$ g min µmol^{-1}) for β-Mo_2N (*filled triangle*) and Au/β-Mo_2N (*open triangle*); lines represent fit to eq. (3). Pseudo-first order kinetic plot for reaction over: **b** β-Mo_2N (*filled triangle*) and Au/β-Mo_2N (*open triangle*); **c** γ-Mo_2N-a (*filled circle*) and Au/γ-Mo_2N-a (*open circle*); **d** γ-Mo_2N-b (*filled square*) and Au/γ-Mo_2N-b (*open square*)

Table 3 *p*-CNB hydrogenation rate constants (k and k')

Catalyst	Rate constant k (µmol g^{-1} min^{-1})	Specific rate constant k' ($\times 10^{-2}$ µmol m^{-2} min^{-1})
β-Mo_2N	4.6	66
γ-Mo_2N-a	12.2	34
γ-Mo_2N-b	24.5	37
Au/β-Mo_2N	9.0	100
Au/γ-Mo_2N-a	20.4	51
Au/γ-Mo_2N-b	38.4	47

β-Mo_2N. This can be correlated with the greater hydrogen content relative to γ-Mo_2N, which, in turn, is related to the increased number of nitrogen deficient (higher Mo/N, see Table 2) surface sites. The results demonstrate that *p*-CNB hydrogenation performance is sensitive to the nitride phase where rate is proportional to surface area.

3.2 Au/Mo_2N

3.2.1 Preparation and Characterisation

Catalyst supports, notably metal oxides, exhibit a characteristic pH-dependent surface charge [76]. The pH associated with the point of zero charge (pH_{PZC}) is a critical property that determines the solution pH requirements to ensure effective precursor-support interactions during catalyst preparation by D–P [77]. When pH < pH_{PZC}, the support bears a positive charge (due to protonation), favouring interaction with anionic species in solution and a pH in excess of pH_{PZC} results in a surface affinity for cationic species [78]. The pH_{PZC} depends on the chemical nature of the support rather than the crystallographic phase with equivalent values recorded for α- and γ-Al_2O_3, TiO_2-rutile and TiO_2-anatase, maghemite (γ-) and hematite (α-Fe_2O_3) [79]. The titration curves associated with pH_{PZC} measurements for β-Mo_2N (1a), γ-Mo_2N-a (1b) and γ-Mo_2N-b (1c) are presented in Fig. 8, yielding a similar value (3.4 ± 0.1) for the three nitrides. We could not find any published work that included a measurement of pH_{PZC} for Mo_2N. The temporal pH variations during the preparation of Au/β-Mo_2N (2a), Au/γ-Mo_2N-a (2b) and Au/γ-Mo_2N-b (2c) are also given in Fig. 8. Initially, solution pH < pH_{PZC} and an electrostatic interaction between anionic gold species in solution ($HAuCl_4$ and/or $Au(OH)Cl_3^-$) and the positively charged support is favoured [38]. The surface sites act as nucleation centres for Au deposition [80]. The progressive decomposition of urea, as a result of the increase in temperature (up to 353 K), led to a gradual increase in solution pH where pH > pH_{PZC}. The support develops a negative surface charge resulting in an electrostatic repulsion with anionic gold species. A combination of chemical and electrostatic interactions between the precipitating species and the support are required to facilitate metal deposition [77]. Moreover, supports with a greater surface area can facilitate a more homogeneous nucleation, resulting in the formation of

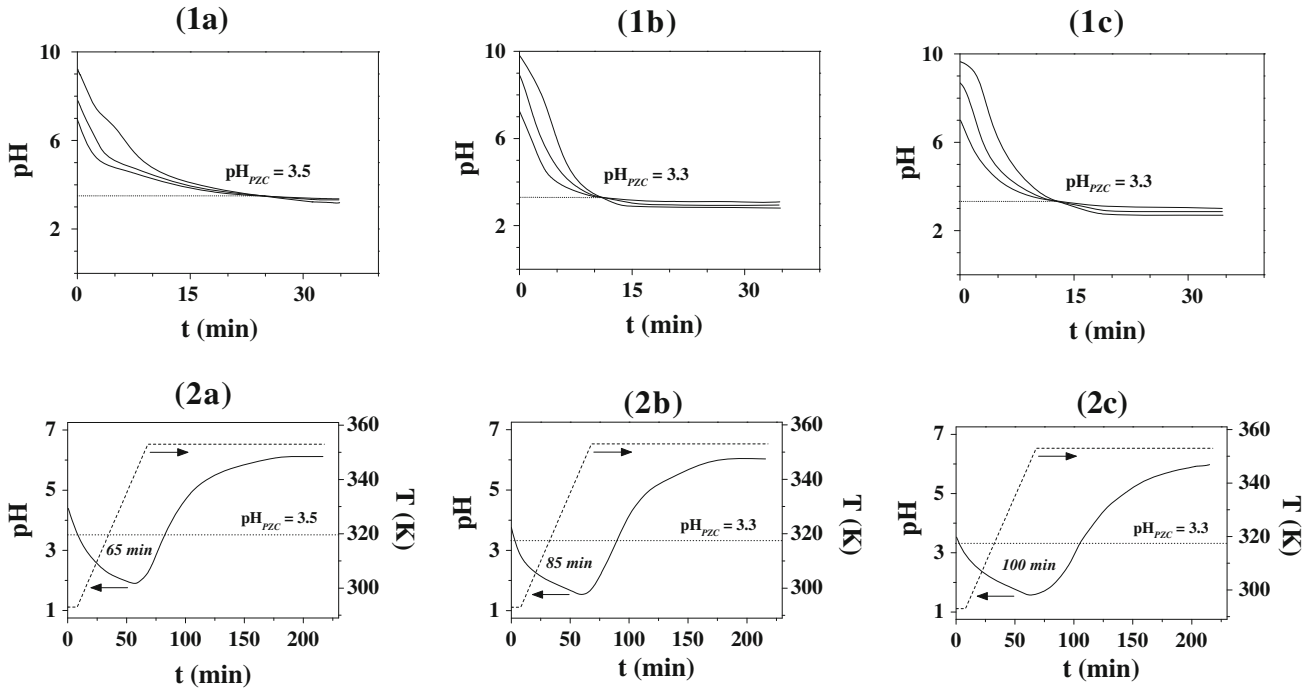

Fig. 8 **1** pH profiles associated with the point of zero charge (pH_{PZC}) determination for *a* β-Mo_2N, *b* γ-Mo_2N-a and *c* γ-Mo_2N-b. **2** Temporal pH (*solid line*) and temperature (*dashed line*) variations in the preparation of *a* Au/β-Mo_2N, *b* Au/γ-Mo_2N-a and *c* Au/γ-Mo_2N-b. *Dotted line* identifies the pH_{PZC} of the nitride; time during which pH < pH_{PZC} is given in *italics*

smaller supported Au ensembles. The ultimate Au loadings (0.26–0.59 mol.%, see Table 2) are below the nominal 1 mol.%, which can be associated with the low pH_{PZC} that characterises the three nitride supports. A similar interpretation was proposed for a lower than expected Au content resulting from deposition on SiO_2 (pH_{PZC} = 2.2) [81]. The range of Au loadings obtained in this study can be correlated to the synthesis time where solution pH < pH_{PZC}, which was shortest (65 min) for β-Mo_2N, representing less favourable conditions for Au deposition resulting in the lowest metal content. The Au loading on both γ-Mo_2N supports with similar times at pH < 3.3 (pH_{PZC}) was essentially equivalent.

A concomitant increase in BET surface area and pore volume was observed after Au inclusion (Table 2). A similar phenomenon has been observed for the deposition of Pd and Au on boron nitride [82] and attributed to the development of nanopores during thermal treatment (drying and activation) with the release of water incorporated during deposition. The TPR profiles associated with Au/β-Mo_2N (a2), Au/γ-Mo_2N-a (b2) and Au/γ-Mo_2N-b (c2) are presented Fig. 4. Each is characterised by a principal H_2 consumption peak with T_{max} = 606 ± 4 K ascribed to passivating layer removal where the incorporation of Au resulted in a decrease in reduction temperature (by up to 60 K, see Fig. 4a1–c1). A similar effect has been noted elsewhere [58] for the TPR of passivated Mo_2N, i.e. shift to lower temperature by up to 140 K, following Ni introduction. Moreover, the incorporation of Au on reducible carriers, e.g. Fe_2O_3 [83] and $Ce_xZr_{1-x}O_2$ [84] has resulted in a significant decrease (by up to 400 K) in the temperature required for partial reduction of the support. Reduction of oxide supported gold ($Au^{3+} \rightarrow Au^0$) prepared by D–P has been reported to generate a TPR peak at $T < 500$ K [67]. This was not a feature of this study, suggesting a transformation of the Au precursor to metallic Au during preparation (pre-TPR). This has been reported previously [85], notably in the synthesis of iron oxide supported Au by co-precipitation. A reductive deposition of Au can occur on surface oxidised Mo species (post-passivation). The significantly lower standard redox potential of ionic Mo (e.g. E^0 for $H_2Mo^{VI}O_4/Mo^{IV}O_2$ = + 0.65 V) compared with ionic Au (E^0 for $Au^{III}(OH)_3/Au^0$ = + 1.32 V, E^0 for $Au^{III}Cl_4^-/Au^0$ = + 1.00 V) [86] can act to reduce the Au precursor. The incorporation of Au was accompanied by greater H_2 consumption during TPR (Table 2). This can be linked to (i) the increase in surface area and (ii) hydrogen spillover (from Au). It is known that H_2 chemisorption on supported Au is limited when compared with platinum group metals [87] but dissociative adsorption can proceed on low coordination Au sites, i.e. at edges and corners [88]. The three Au/nitride samples exhibited a measurable increase in H_2 chemisorption relative to the nitride support (Table 2). Hydrogen TPD generated the profiles shown in Fig. 5 for Au/β-Mo_2N (a2), Au/γ-Mo_2N-a (b2) and Au/γ-Mo_2N-b

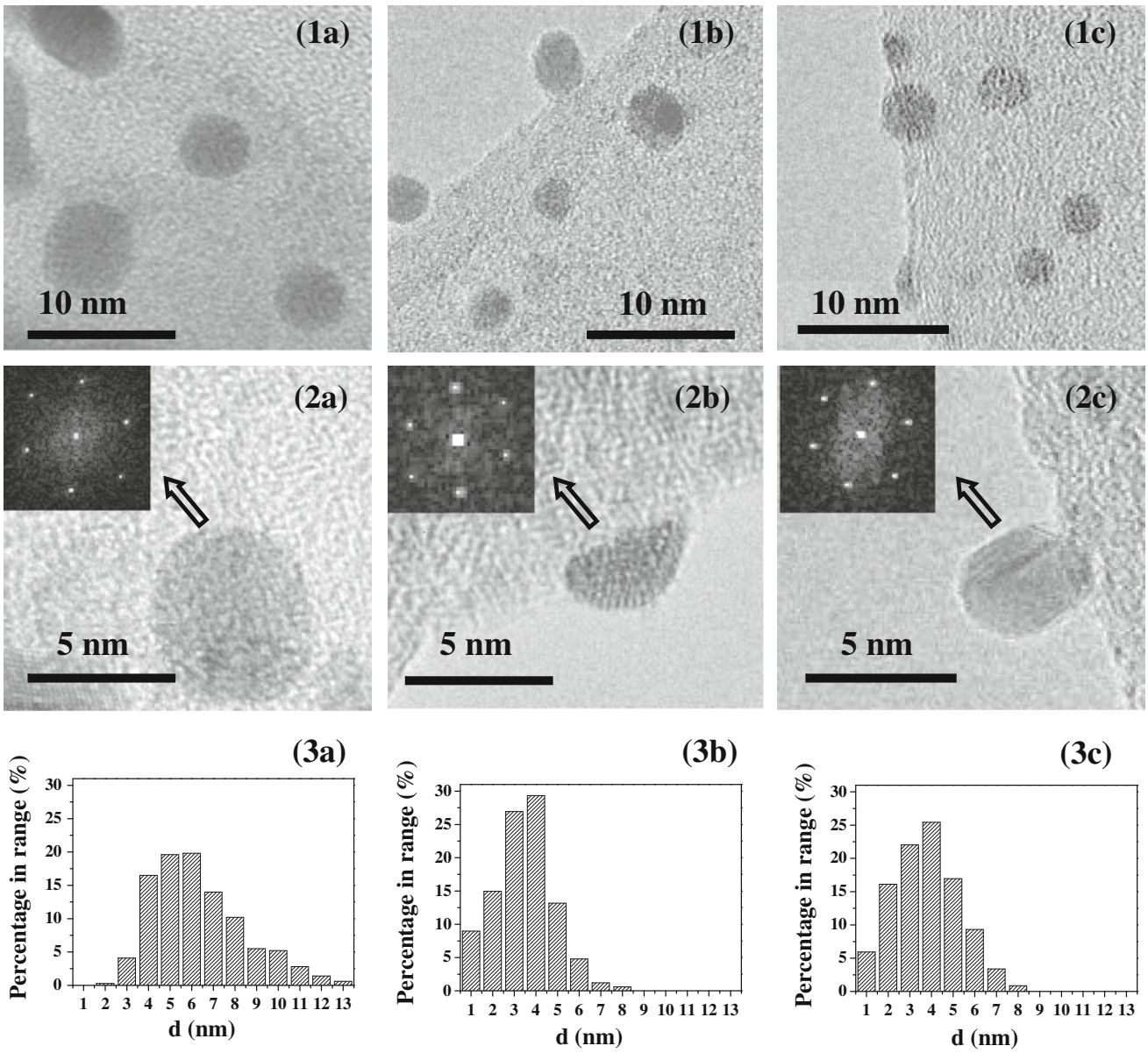

Fig. 9 Representative **1** medium and **2** high magnification TEM images and **3** Au particle size distribution associated with *a* Au/β-Mo_2N, *b* Au/γ-Mo_2N-a and *c* Au/γ-Mo_2N-b. *Insets* in high magnification TEM images show diffractogram patterns for single Au particles

(c2). In each case, the incorporation of Au resulted in a significant increase in the amount of H_2 released (see Table 2). The TPD profiles present a principal peak (746–813 K) at a lower temperature (by up to 60 K) than that recorded for the nitride with an additional higher temperature (933 K) shoulder. These results indicate that the addition of Au results in greater capacity for hydrogen uptake (and subsequent release) with a distinct TPD response relative to the starting nitride.

Transmission electron microscopy was employed to obtain a measure of Au particle size. Representative (1) medium and (2) high magnification TEM images with particle size distributions (3) for (a) Au/β-Mo_2N, (b) Au/γ-Mo_2N-a and (c) Au/γ-Mo_2N-b are presented Fig. 9. The images reveal a well dispersed Au phase in the form of quasi-spherical nano-scale particles. The diffractogram patterns for isolated Au particles are included (as insets) in the high magnification images (2) where the *d*-spacings (0.20/0.23) are consistent with the (111) and (200) planes of metallic gold. For the three catalysts, the Au particles (number average mean of 4–7 nm) are predominantly within the size range ($\leq$10 nm) that has been deemed critical for hydrogenation activity [89]. The smaller mean Au size associated with γ-Mo_2N (see Table 2) can be

ascribed to the prolonged deposition time where pH < pH_{PZC} (see Fig. 8), resulting in stronger interactions with the support that minimise particle agglomeration.

3.2.2 Catalytic Results

The chemoselective hydrogenation of nitro-compounds over oxide supported Au is now established [61, 62, 90]. It has been shown that Au catalysts preferentially promote N=O reduction over other reactive functional groups, such as C≡N [91], C=O [90], C=C [62], Br [75] and Cl [92]. Activity and selectivity are dependent on Au particle size [93] and the nature of the support [61]. In the gas phase hydrogenation of *p*-CNB, we have demonstrated exclusive nitro-group reduction over Au supported on non-reducible (SiO_2, Al_2O_3) [94] and reducible (CeO_2, TiO_2, Fe_2O_3) [92] carriers. The results of this study demonstrate that this chemoselective response extends to Au supported on β-Mo_2N and γ-Mo_2N where reaction exclusivity to *p*-CAN was maintained. Moreover, incorporation of Au enhanced hydrogenation performance, as shown in Fig. 7, where the specific rate delivered by Au/β-Mo_2N exceeded that obtained with both Au/γ-Mo_2N (Table 3). Increased activity due to Au inclusion can be linked to an increase in reactive hydrogen as established by TPD analysis.

4 Conclusions

Temperature programmed treatment of MoO_3 in flowing $N_2 + H_2$ was used to synthesise tetragonal β-Mo_2N (7 $m^2\ g^{-1}$) and cubic γ-Mo_2N (36 and 66 $m^2\ g^{-1}$). The γ-form exhibits a platelet (ca. 15 × 25 μm^2) morphology whereas β-Mo_2N takes the form of aggregates of small (<5 μm) crystallites. Passivation of the synthesised samples provided a protective oxide layer that prevented bulk oxidation and facilitated *ex-situ* handling. In the synthesis of Au/Mo_2N, solution pH exceeded support pH_{PZC} (3.4 ± 1) resulting in a less favourable surface interaction with the anionic Au precursor. This was particularly pronounced in the case of β-Mo_2N and resulted in lower Au loading and the formation of larger Au particles (mean diameter = 7 nm for Au/β-Mo_2N vs. 4 nm for Au/γ-Mo_2N) after activation. TPR to 673 K was necessary to remove the passivation layer where the inclusion of Au shifted the TPR profile to lower temperatures (by up to 60 K). 100 % selectivity to the target *p*-CAN product in the hydrogenation of *p*-CNB was achieved over Mo_2N, regardless of the phase. Hydrogen TPD analysis has established H_2 uptake on each nitride during TPR where β-Mo_2N exhibited a higher specific (per unit area) H_2 content relative to γ-Mo_2N. This is associated with a greater number of nitrogen deficient sites on β-Mo_2N (as established by XPS analysis), which translates into a higher specific selective hydrogenation rate. An equivalent specific rate was obtained for both γ-Mo_2N samples, indicative of invariance with respect to surface area. The addition of Au served to increase H_2 uptake capacity and elevated hydrogenation rate where *p*-CAN was again the sole product; Au/β-Mo_2N outperformed Au/γ-Mo_2N. Our results demonstrate that the combination of Au with Mo_2N is a viable catalyst formulation for selective nitroarene hydrogenation.

Acknowledgments This work was financially supported by EPSRC (Grant 0231 110525) and the Swiss National Science Foundation (Grant 200020-132522/1). EPSRC support for free access to the TEM/SEM facility at the University of St Andrews is also acknowledged.

References

1. Alexander AM, Hargreaves JSJ (2010) Chem Soc Rev 39: 4388–4401
2. Furimsky E (2003) Appl Catal A 240:1–28
3. Nagai M (2007) Appl Catal A 322:178–190
4. Wu Z, Yang S, Xin Q, Li C (2003) Catal Surv Asia 7:103–119
5. Hao ZX, Wei ZB, Wang LJ, Li XH, Li C, Min EZ, Xin Q (2000) Appl Catal A 192:81–84
6. Guerrero-Ruiz A, Zhang Y, Bachiller-Baeza B, Rodríguez-Ramos I (1998) Catal Lett 55:165–168
7. Li Y, Fan Y, He J, Xu B, Yang H, Miao J, Chen Y (2004) Chem Eng J 99:213–218
8. Cárdenas-Lizana F, Gómez-Quero S, Perret N, Kiwi-Minsker L, Keane MA (2011) Catal Sci Technol 1:794–801
9. Neylon MK, Choi S, Kwon H, Curry KE, Thompson LT (1999) Appl Catal A 183:253–263
10. Eberhart ME, MacLaren JM (1996) In: Oyama ST (ed) The chemistry of transition metal carbides and nitrides. Blackie, Glasgow
11. Cárdenas-Lizana F, Gómez-Quero S, Perret N, Kiwi-Minsker L, Keane MA (2012) Catal Commun 21:46–51
12. Cárdenas-Lizana F, Lamey D, Gómez-Quero S, Perret N, Kiwi-Minsker L, Keane MA (2011) Catal Today 173:53–61
13. SIDS Initial Assessment report for 15th SIAM OECD SIDS (2002) 1-4-chloronitrobenzene, CAS N° 100-00-15. UNEP publications
14. Li S, Kim WB, Lee JS (1998) Chem Mater 10:1853–1862
15. Nagai M, Goto Y, Uchino O, Omi S (1998) Catal Today 43:249–259
16. Markel EJ, Burdick SE, Leaphart ME, Roberts KL (1999) J Catal 182:136–147
17. Wei ZBZ, Grange P, Delmon B (1998) Appl Surf Sci 135:107–114
18. McKay D, Hargreaves JSJ, Rico JL, Rivera JL, Sun XL (2008) J Solid State Chem 181:325–333
19. Gong S, Chen H, Li W, Li B (2005) Appl Catal A 279:257–261
20. Cairns AG, Gallagher JG, Hargreaves JSJ, McKay D, Morrison E, Rico JL, Wilson K (2009) J Alloy Compd 479:851–854
21. Roberts KL, Markel EJ (1994) J Phys Chem 98:4083–4086
22. Wise RS, Markel EJ (1994) J Catal 145:344–355
23. Marchand R, Tessier F, DiSalvo FJ (1999) J Mater Chem 9:297–304
24. Choi J-G, Curl RL, Thompson LT (1994) J Catal 146:218–227

25. Jaggers CH, Michaels JN, Stacy AM (1990) Chem Mater 2:150–157
26. McGee RCV, Bej SK, Thompson LT (2005) Appl Catal A 284:139–146
27. Volpe L, Boudart M (1985) J Solid State Chem 59:332–347
28. Wei ZB, Xin Q, Grange P, Delmon B (1997) J Catal 168:176–182
29. Li XS, Chen YX, Zhang YJ, Ji CX, Xin Q (1996) React Kinet Catal Lett 58:391–396
30. Choi JG, Lee HJ, Thompson LT (1994) Appl Surf Sci 78: 299–307
31. Colling CW, Choi J-G, Thompson LT (1996) J Catal 160:35–42
32. Setthapun W, Bej SK, Thompson LT (2008) Top Catal 49:73–80
33. Logan JW, Heiser JL, McCrea KR, Gates BD, Bussell ME (1998) Catal Lett 56:165–171
34. Xie GH, Jiang ZC (2000) Chin Sci Bull 45:1562–1564
35. Peck JA, Tait CD, Swanson BI, Brown GE (1991) Geochim Cosmochim Acta 55:671–676
36. Dobrosz I, Jiratova K, Pitchon V, Rynkowski JM (2005) J Mol Catal A 234:187–197
37. Oh HS, Yang JH, Costello CK, Wang YM, Bare SR, Kung HH, Kung MC (2002) J Catal 210:375–386
38. Zanella R, Louis C (2005) Catal Today 107:768–777
39. Vakros J, Kordulis C, Lycourghiotis A (2002) Chem Commun 17:1980–1981
40. Gong SW, Chen HK, Li W, Li BQ (2006) Energy Fuels 20: 1372–1376
41. Nagai M, Goto Y, Miyata A, Kiyoshi M, Hada K, Oshikawa K, Omi S (1999) J Catal 182:292–301
42. de Lucas Consuegra A, Patterson PM, Keane MA (2006) Appl Catal B 65:227–239
43. Sloczynski J, Bobinski W (1991) J Solid State Chem 92:436–448
44. McKay D, Hargreaves JSJ, Howe RF (2006) Catal Lett 112:109–113
45. Aouadi SM, Paudel Y, Luster B, Stadler S, Kohli P, Muratore C, Hager C, Voevodin AA (2008) Tribol Lett 29:95–103
46. Cai PJ, Yang ZH, Wang CY, Gu YL, Qian YT (2005) Chem Lett 34:1360–1361
47. Inumaru K, Baba K, Yamanaka S (2005) Chem Mater 17:5935–5940
48. Gong SW, Chen HK, Li W, Li BQ (2004) Catal Commun 5:621–624
49. Panda RN, Kaskel S (2006) J Mater Sci 41:2465–2470
50. Haddix GW, Reimer JA, Bell AT (1987) J Catal 108:50–54
51. Li XS, Zhang KJ, Xin Q, Ji CX, Miao YF, Wang L (1996) React Kinet Catal Lett 57:177–182
52. Zhang Y, Xin Q, Rodriguez-Ramos I, Guerrero-Ruiz A (1999) Mater Res Bull 34:145–156
53. Dewangan K, Patil SS, Joag DS, More MA, Gajbhiye NS (2010) J Phys Chem C 114:14710–14715
54. Shi C, Zhu AM, Yang XF, Au CT (2004) Catal Lett 97:9–16
55. Choi J-G, Choi D, Thompson LT (1997) Appl Surf Sci 108: 103–111
56. Qi J, Jiang LH, Jiang QA, Wang SL, Sun GQ (2010) J Phys Chem C 114:18159–18166
57. He H, Dai HX, Ngan KY, Au CT (2001) Catal Lett 71:147–153
58. Wang YH, Li W, Zhang MH, Guan NJ, Tao KY (2001) Appl Catal A 215:39–45
59. Li XS, Sheng SS, Chen HR, Ji CX, Zhang YJ, Xin Q (1995) Acta Phys Chim Sin 11:678–680
60. Nagai M, Omi S (1995) Sekiyu Gakkaishi 38:363–373
61. Blaser H-U, Steiner H, Studer M (2009) ChemCatChem 1: 210–221
62. Corma A, Gonzalez-Arellano C, Iglesias M, Sanchez F (2009) Appl Catal A 356:99–102
63. Wang XD, Liang MH, Zhang JL, Wang Y (2007) Curr Org Chem 11:299–314
64. Kanth SR, Reddy GV, Rao VVVNSR, Maitraie D, Narsaiah B, Rao PS (2002) Synth Commun 32:2849–2853
65. Sonavane SU, Gawande MB, Deshpande SS, Venkataraman A, Jayaram RV (2007) Catal Commun 8:1803–1806
66. Xiong J, Chen JX, Zhang JY (2007) Catal Commun 8:345–350
67. Cárdenas-Lizana F, Gómez-Quero S, Perret N, Keane MA (2011) Catal Sci Technol 1:652–661
68. Corma A, Serna P, Concepcion P, Calvino JJ (2008) J Am Chem Soc 130:8748–8753
69. Chen YZ, Chen YC (1994) Appl Catal A 115:45–57
70. Coq B, Tijani A, Figueras F (1991) J Mol Catal 68:331–345
71. Tijani A, Coq B, Figueras F (1991) Appl Catal 76:255–266
72. Vishwanathan V, Jayasri V, Basha PM, Mahata N, Sikhwivhilu L, Coville NJ (2008) Catal Commun 9:453–458
73. Ren J, Wang JG, Huo CF, Wen XD, Cao Z, Yuan SP, Li YW, Jiao HJ (2007) Surf Sci 601:1599–1607
74. Deiner LJ, Kang DH, Friend CA (2005) J Phys Chem B 109:12826–12831
75. Cárdenas-Lizana F, Gómez-Quero S, Keane MA (2008) Catal Commun 9:475–481
76. Kosmulski M (2001) Chemical properties of material surfaces, surfactant science series vol 102. Marcel Dekker, New York
77. Geus JW, van Dillen AJ (1999) In: Ertl G, Knözinger H, Weitkamp J (eds) Preparation of solid catalysts. Wiley-VCH, Weinheim
78. Moreau F, Bond GC (2007) Catal Today 122:260–265
79. Kosmulski M (2009) Adv Colloid Interface Sci 152:14–25
80. Moreau F, Bond GC, Taylor AO (2005) J Catal 231:105–114
81. Somodi F, Borbath I, Hegedus M, Tompos A, Sajo IE, Szegedi A, Rojas S, Fierro JLG, Margitfalvi JL (2008) Appl Catal A 347:216–222
82. Postole G, Gervasini A, Guimon C, Auroux A, Bonnetot B (2006) J Phys Chem B 110:12572–12580
83. Silberova BAA, Mul G, Makkee M, Moulijn JA (2006) J Catal 243:171–182
84. Collins SE, Cíes JM, del Río E, López-Haro M, Trasobares S, Calvino JJ, Pintado JM, Bernal S (2007) J Phys Chem C 111:14371–14379
85. Hodge NA, Kiely CJ, Whyman R, Siddiqui MRH, Hutchings GJ, Pankhurst QA, Wagner FE, Rajaram RR, Golunski SE (2002) Catal Today 72:133–144
86. Greenwood NN, Earnshaw A (1997) Chemistry of the elements, 2nd edn. Butterworth-Heinemann, Oxford
87. McEwan L, Julius M, Roberts S, Fletcher JCQ (2010) Gold Bull 43:298–306
88. Claus P, Hofmeister H, Mohr C (2004) Gold Bull 37:181–186
89. Bond G, Louis C, Thompson DT (2006) Catalysis by gold. Imperial College Press, London
90. Corma A, Serna P (2006) Science 313:332
91. Corma A, Serna P (2006) Nat Protoc 1:2590–2595
92. Cárdenas-Lizana F, Gómez-Quero S, Perret N, Keane MA (2009) Gold Bull 42:124–132
93. Corma A, Garcia H (2008) Chem Soc Rev 37:2096–2126
94. Cárdenas-Lizana F, Gómez-Quero S, Keane MA (2008) ChemSusChem 1:215–221